Article

Current Biology

A quantitative morphospace of multicellular organ design in the plant *Arabidopsis*

Highlights

- Cellular configurations arising by chance are explored using 3D digital tissue models
- Generation of a 3D cellular-resolution tissue dataset of *Arabidopsis*
- Apical stem cell niche most closely resembles default cellular packing
- Leaf and sepal are the most complex tissues due to air spaces and elongated cells

Authors

Salva Duran-Nebreda, Matthew D.B. Jackson, George W. Bassel

Correspondence

george.bassel@warwick.ac.uk

In brief

Duran-Nebreda et al. investigate the diversity of cellular configurations in plant organs. Digital 3D cellular-resolution tissue models were compared with a 3D digital atlas of *Arabidopsis* tissues. A gradient of organ complexity was established, with stem cells being closest to the default and leaves and sepals being the most complex organs.

Duran-Nebreda et al., 2023, Current Biology *33*, 4798–4806
November 20, 2023
https://doi.org/10.1016/j.cub.2023.09.048

CellPress

CellPress
OPEN ACCESS

Current Biology

Article

A quantitative morphospace of multicellular organ design in the plant *Arabidopsis*

Salva Duran-Nebreda,[1] Matthew D.B. Jackson,[1] and George W. Bassel[1,2,*]
[1]School of Life Sciences, University of Warwick, Coventry CV4 7AL, UK
[2]Lead contact
*Correspondence: george.bassel@warwick.ac.uk
https://doi.org/10.1016/j.cub.2023.09.048

SUMMARY

Organ function emerges from the interactions between their constituent cells. The investigation of cellular organization can provide insight into organ function following structure-function relationships. Here, we investigate the extent to which properties in cellular organization can arise "for free" as an emergent property of embedding cells in space versus those that are actively generated by patterning processes. Default cellular configurations were established using three-dimensional (3D) digital tissue models. Network-based analysis of these synthetic cellular assemblies established a quantitative topological baseline of cellular organization, granted by virtue of passive spatial packing and the minimal amount of order that emerges for free in tessellated tissues. A 3D cellular-resolution digital tissue atlas for the model plant species *Arabidopsis* was generated, and the extent to which the organs in this organism conform to the default configurations was established through statistical comparisons with digital tissue models. Cells in different tissues of *Arabidopsis* do not conform to random packing arrangements to varying degrees. Most closely matching the random models was the undifferentiated shoot apical meristem (SAM) from which aerial organs emanate. By contrast, leaf and sepal tissue showed the greatest deviation from this baseline, suggesting these to be the most "complex" tissues in *Arabidopsis*. Investigation of the patterning principles responsible for the gap between these tissues and default patterns revealed cell elongation and the introduction of air spaces to contribute toward additional organ patterning complexity. This work establishes a quantitative morphospace to understand the principles of organ construction and its diversity within a single organism.

INTRODUCTION

Since the emergence of multicellular organisms, an increase in complexity has been shown to operate across multiple scales and domains of life.[1–4] One example of this is the advent of novel cell types.[1] This has been conflated to the capacity of organisms to carry out novel biological processes and functions and the ability to occupy new ecological niches.[5,6]

Functionality in multicellular systems may also emerge from structure-function relationships in terms of the configurations of the cells that make up organs.[7,8] The relative position of cells and cell types in space confers tissues with specific biophysical as well as biochemical properties. This is illustrated by the misplacement of cells in tissues underpinning many diseases and critical developmental processes, such as cancer,[9–11] mechanical deformation during development,[12] and brain development.[13]

Control of the spatial arrangement of cells in plants is particularly pertinent, as cells that share a cell wall cannot reconfigure relative to one other once a pattern has been established.[14,15]

Toward understanding emergent organ function, a quantitative understanding of the cellular configurations from which they are constructed can be pursued. Mapping cellular connectivity with a view to understanding system function has been performed previously in nervous systems.[8,16] The application of network science-based analyses of these cellular interaction networks has proven useful in understanding both system-level function and the role of individual cells.[8,17] Cellular connectivity mapping and network science have also been used to uncover putative structure-function relationships in plant tissues,[18–20] providing a path to understanding quantitative organ design principles outside of nervous systems.

This study seeks to understand the organizational properties of cells embedded in three-dimensional (3D) space. Specifically, which topological properties passively emerge due to the inherent properties of cells packed in space (complexity for free[21]) versus those that are generated by active patterning mechanisms. We address this question by taking a quantitative network-based methodology to investigate multicellular organization to quantify the spatial relationships of cells embedded in 3D space. Using this approach, cells are considered nodes within a graph, connected by edges if there is a shared physical boundary between them. We build three families of virtual organ models that make use of isotropic tessellations of centroid point clouds.[22] These models provide a baseline for the cellular configurations that can arise due to 3D cell packing and identify topological features associated with them. Comparison of these computationally generated organs with cellular connectomes derived from the plant *Arabidopsis* identified the extent to which active patterning leads to the construction of different organs in this species.

RESULTS

Generation of a 3D digital single-cell atlas of *Arabidopsis* tissues

The model plant *Arabidopsis* generates a diversity of tissues. We sought to quantitatively analyze the diversity of cellular configurations in this organism through the generation of a 3D digital single-cell atlas. Comprehensive digital capture of cells in tissues and their abstraction into connectivity networks enabled quantitative approaches using network science to be pursued.[23]

Fully mature tissues were sampled, representing a morphometric analysis of the endpoint of developmental patterning processes.[7] Tissues examined included the shoot apical meristem (SAM) (representing the apical stem cell niche), the mature root, the leaf (Figure 1A), the hypocotyl (stem from a seedling), the flower components (anther, filament, pedicel, and sepal), and maternal fruit tissue named the valve (Figure 1B). These represent a broad sampling of the tissues produced by this model plant species.

Generation of quantitative organ cellular patterning morphospaces

The quantitative relationship between cellular organization in *Arabidopsis* organs was examined using a quantitative topological morphospace. This organ design space made use of connectomes describing global cellular connectivity and consists of two dimensions: local efficiency and global efficiency.[24]

Local efficiency deals with the impact of random failure of nodes in the local increase of shortest path lengths between pairs of nodes. This describes the resilience of a network to random errors in terms of increased costs of transportation locally. Global efficiency deals with the efficient routing of information across the whole network. This is calculated by considering the shortest paths between all pairs of nodes, addressing how easily information can move across a given network. As the networks analyzed were subsampled to control for their size, we term this normalized global efficiency. A trade-off between communication efficiencies at these scales is therefore present and represents a well-established means of analyzing spatially constrained transport networks,[25] including a multicellular organ.

The normalized global efficiency of different *Arabidopsis* tissues is relatively constant, suggesting that they are robust to information transfer at this scale (Figure 1C). By contrast, differences in local efficiency are observed, suggesting a varying capacity to buffer local communication efficiency against the loss of individual cells across tissues. The ratio of epidermal to internal cells in tissues did not have a large impact on degree or transport efficiency (Figures S1A–S1C).

Generation of 3D virtual organ models

In order to explore the topological landscape that cells embedded in 3D space occupy, a series of geometric, spatially embedded models were developed. These models use isotropic 3D Voronoi tessellation originating from computationally positioned centroids to create "virtual organs" consisting of interconnected cells.[26] The creation of these virtual organ prototypes started with a set of centroids in 3D space, each representing a single cell, which is expanded simultaneously in all directions. Where two of these expanding centroids meet, a physical contact between cells is created, delimiting the boundary of the cells as well as providing an edge for the network formalism that we use in this study. Different approaches to centroid positioning were used to generate a diversity of multicellular topologies.

The space used to generate virtual organ models was constrained using a sphere that encapsulated the space within which the cells are created (Figure 2A).

Method A: Random centroid positioning models

In the first series of models, iterative random positioning of centroids was performed. The three coordinates for the centroid positions were drawn from a uniform distribution of matching size to the diameter of the sphere. Centroids lying within the sphere were accepted, whereas centroids located outside the sphere boundary were rejected (Figure 2A). This process was carried out until a certain number of centroids was reached, from 4 to 512 nodes/cells (Figures 2B and 2C). With the centroids positioned, a deterministic isotropic 3D Voronoi tessellation was carried out in order to define the volumes corresponding to each cell.[27] Upon construction of the cellular volumes, a network was extracted, with nodes representing cells and edges representing physical connections between them.

In the extracted networks representing cellular connectivity, the relationship between the number of nodes and edges in networks of increasing size was examined. A linear correlation was observed in a log-log plot (Figure 2B), suggesting that this relationship is scale invariant, a property observed in many randomly generated networks.[28]

For each of the random centroid position networks, cell topological properties were analyzed using degree (number of neighbors a cell has) (Figure 2C), betweenness centrality, and random-walk centrality (how many shortest paths the cell lies upon in the multicellular network) (Figures 2D, 2E, and S1).[23] Increasing the number of cells led to large topological variability in models with respect to betweenness centrality and random-walk centrality, indicating that these local and global properties are variant across different organ sizes in this model class.

Method B: Noisy perturbation of ordered centroid lattices

This second class of model started from ordered lattices of cell centroids and perturbing their positions with increasing amounts of variability to overcome the order of this configuration (Figure 2F). The modeling process started with an ordered set of 512 centroids within a sphere. The centroids were then separated 10 μm in the X- and Y- directions and staggered in the Z direction, forming a regular structure similar to those obtained from the optimal packing of spheres in 3D.[29] This configuration can be tessellated to obtain perfectly ordered lattices, with 12 neighbors per node (Figures 2G and S2). However, slight changes in the starting position of the centroids give rise to different systems in terms of the local and global properties discussed before (Figures 2H–2J and S2), even when breaking the initial symmetry by a relatively small perturbation.[29]

Increasing the amount of noise applied to centroid positions led to an increased degree (Figure 2H) and coefficient of variance in degree (Figure 2I). The random-walk centrality of these models also decreased with increasing amounts of noise, whereas the

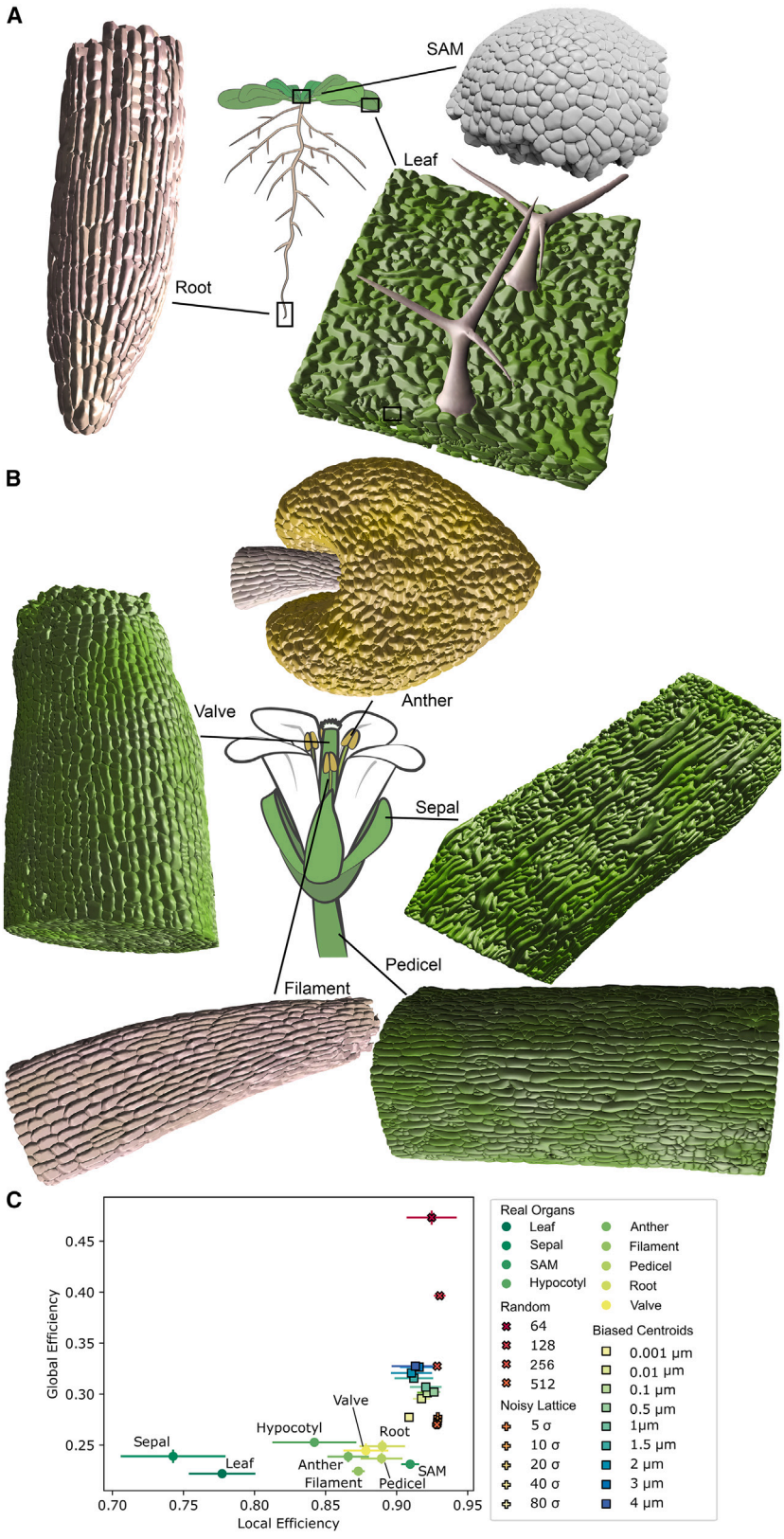

Figure 1. A quantitative morphospace of cellular organization in *Arabidopsis* organs

3D renderings of *Arabidopsis* organs imaged and analyzed in this study

(A) Tissues from the vegetative plant and (B) from the flower. Samples were segmented at cellular resolution in 3D and false colored. Cells are not drawn to scale. *Arabidopsis* plant graphic in (A) and flower in (B) adapted from Bouché 2018, https://figshare.com/articles/2018_Arabidopsis_flowering_plant/7159937 and https://figshare.com/articles/Flower_Arabidopsis_2018/7159928.

(C) Quantitative morphospace showing the local and global transport efficiencies of real organs and each of the three model classes generated. Error bars represent one standard deviation of the sample. See also Figures S1–S3.

CellPress
OPEN ACCESS

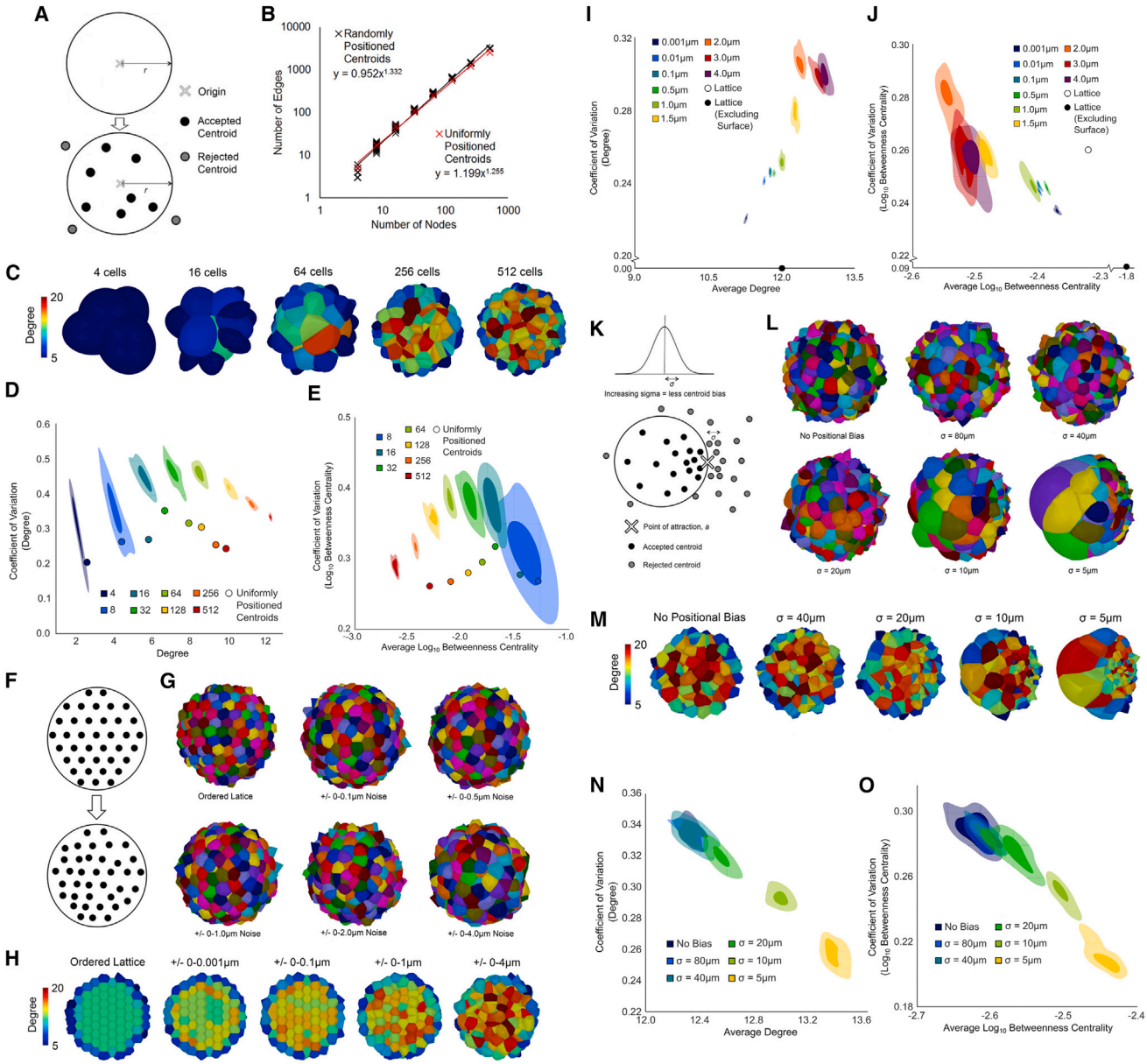

Figure 2. Identification of default cellular configurations using virtual 3D organ models

Construction of 3D digital organ prototypes using different centroid positioning and Voronoi tessellations

(A) Schematic showing construction of random centroid positioning. Centroids are placed randomly in space, and only those within a sphere are retained.

(B) Plot showing relationship between numbers of nodes and edges in random centroid position models.

(C) Spatial distribution of degree (number of neighbors) in different size random centroid position models on organ surface and cross-sections.

(D and E) (D) Relationship between coefficient of variation in degree for the random centroid model and (E) betweenness centrality.

(F) Schematic showing construction of noisy centroid position models.

(G) Voronoi organ models with different amounts of centroid noise.

(H) Spatial distribution of the number of neighbors in models with varying amounts of centroid noise in organ cross-sections.

(I) Same as (D) for the noisy centroid allocation model.

(J) Same as (E) for the noisy centroid allocation model.

(K) Schematic showing method used to spatially bias centroid position in skewed centroid position models.

(L) Voronoi organ models with different amounts of centroid position skew.

(M) Spatial distribution of the number of neighbors in models with varying amounts of centroid position skewing in organ cross-sections.

(N) Same as (D) for the skewed centroid position model.

(O) Same as (E) for the skewed centroid position model. 30 independent subsamples were generated for each of the organs. See also Figures S1–S3.

variability of this measure increased (Figure S2), indicating a progressive convergence in path length and its robustness. The variance in path length, as measured by betweenness centrality and random-walk centrality, remained relatively constant (Figures 2J and S2).

Method C: Biased positioning of centroids

Although some tissues are ordered and lattice-like in nature, this does not capture the full diversity of cell positioning observed in organs. Examples of organs that deviate from these models include cells in different layers of the radially symmetrical *Arabidopsis* root, which are not spaced evenly in the longitudinal axis but are regularly spaced in the radial orientation,[30] and giant cells in plant sepals.[31] To explore the effects of this asymmetric cell positioning on local and global cellular connectivity, an additional set of models was constructed looking at non-uniform cell distributions.

Centroids were positioned in a random and biased manner by placing them following a normal distribution rather than uniform distribution (Figure 2K). Using a normal distribution ensures that cell positioning is not uniform within the synthetic organ: close to the center of the distribution, coordinates are more likely to be chosen, leading to a higher density of centroids.

The X, Y, and Z coordinates were drawn from a normal distribution centered at the boundary of a target sphere. Like the first model, centroids located outside the sphere were discarded, whereas centroids inside the sphere were kept until 512 valid centroids were selected. Different values of σ were used to generate Gaussian distributions for centroid sampling around an identical mean, resulting in 3D Voronoi tessellation models with increasingly biased cell position toward one pole of the organ (Figure 2L).

Greater bias in centroid position led to increases in average degree (Figure 2M) and decreased coefficients of variation in this same measure (Figures 2N and S2). A diminished coefficient of variation was also observed in the betweenness centrality (Figure 2O) and random-walk centrality of increasingly skewed models (Figure S2). The use of biased centroid positions also led to a broader distribution of cell sizes as compared with the other two model classes (Figure S3).

Quantitative comparison on default cellular configurations with multicellular complexity in a plant species

Virtual digital tissue models and their analysis using network science provide a developmental patterning baseline describing the organizational features that can emerge in complex assemblies of cells in the absence of active processes. We sought to examine the extent to which cellular topologies in a complex living organism deviate from these baseline organ designs.

In contrast to the tissue topologies in *Arabidopsis* organs, each of the three classes of models had a relatively constant local efficiency and varying global efficiencies (Figure 1C). None of the models closely reproduced the real organs in terms of both efficiency parameters. This suggested that the topological features conferred to multicellular assemblies through random cellular configurations are not observed in this plant species, and additional patterning processes beyond mere cellular packing are involved in plant tissue formation.

Modification of random geometric models through cell deletion and fusion

The inability of the random geometric models to fully recapitulate observed tissue topologies in *Arabidopsis* prompted the question as to which aspects of the models diverged from configurations observed in nature.

Iterations of 3D Voronoi tessellation create virtual "tissues," which are roughly the same size and extend approximately equally in all directions from their centroids. This accurately reflects the cellular packing that makes up tissues, which are under the constraints of mechanical interactions with their neighbors.[14,32]

Plant tissues sometimes deviate from these tessellated models in 2 primary ways. The first is the presence of cell types that are elongated relative to their neighbors. Examples of this include the root cap, some leaf epidermal cells, and giant cells in sepals.[31,33] Elongated cells are not present in the models generated. Although the third class of random model with biased centroid positioning created a non-uniform cell density and cell size distribution (Figure S4D), the larger cells were isotropic in shape owing to their generation following a 3D Voronoi process, which grows equally in every direction.

The second way in which plant tissues deviate from these models is in the presence of air spaces. Many plant tissues contain gaps within them, including photosynthetic tissues such as leaves and sepals,[34] which facilitate gas exchange with internal mesophyll cells.

Additional organ models were generated, which include each elongated cell and air space. This was achieved by either fusing or deleting virtual cells, respectively (Figure 3A).

The noisy centroid position model with 0.001 μm noise was selected as the baseline model as it most closely represented observed plant tissue topologies (Figure 1C). Fusion and deletion were carried out in two ways. First, using a 512-celled model as a template, node fusion and deletion were performed, reaching variable numbers of final cells (Figure 3B). Additionally, starting from a model with an appropriate number of extra cells, different fractions of cells were randomly deleted, reaching 256 final nodes (Figure 3C). These altered networks were plotted onto the quantitative plant organ morphospace based on local and global transport efficiency, comparing them with real tissues downsampled to 256 cells.

Progressive cell fusion made these models increasingly dissimilar to observed tissues, shifting tissue transport properties to greater normalized global efficiency values (Figure 3C). This may be a consequence of networks becoming easier to traverse through newly formed high-degree links (Figure 3D), whereas local efficiency remained largely unchanged. Similar results were observed when either the random packing (Figure S4) or position bias models (Figure S4) were used as starting points. In light of cell fusion functioning to create elongated cells, their lack of impact on local transport efficiency reflects the observation that sepals lacking giant cells are observed and remain functional.[31]

By contrast, cell deletion led to large relative decreases in local efficiency and modest decreases in normalized global efficiency (Figure 3B). Virtual organ models are therefore sensitive to loss of cells (random failure), making them more difficult to traverse. Deletion of cells brought organ models closer into the morphospace range occupied by plant organs than node fusion

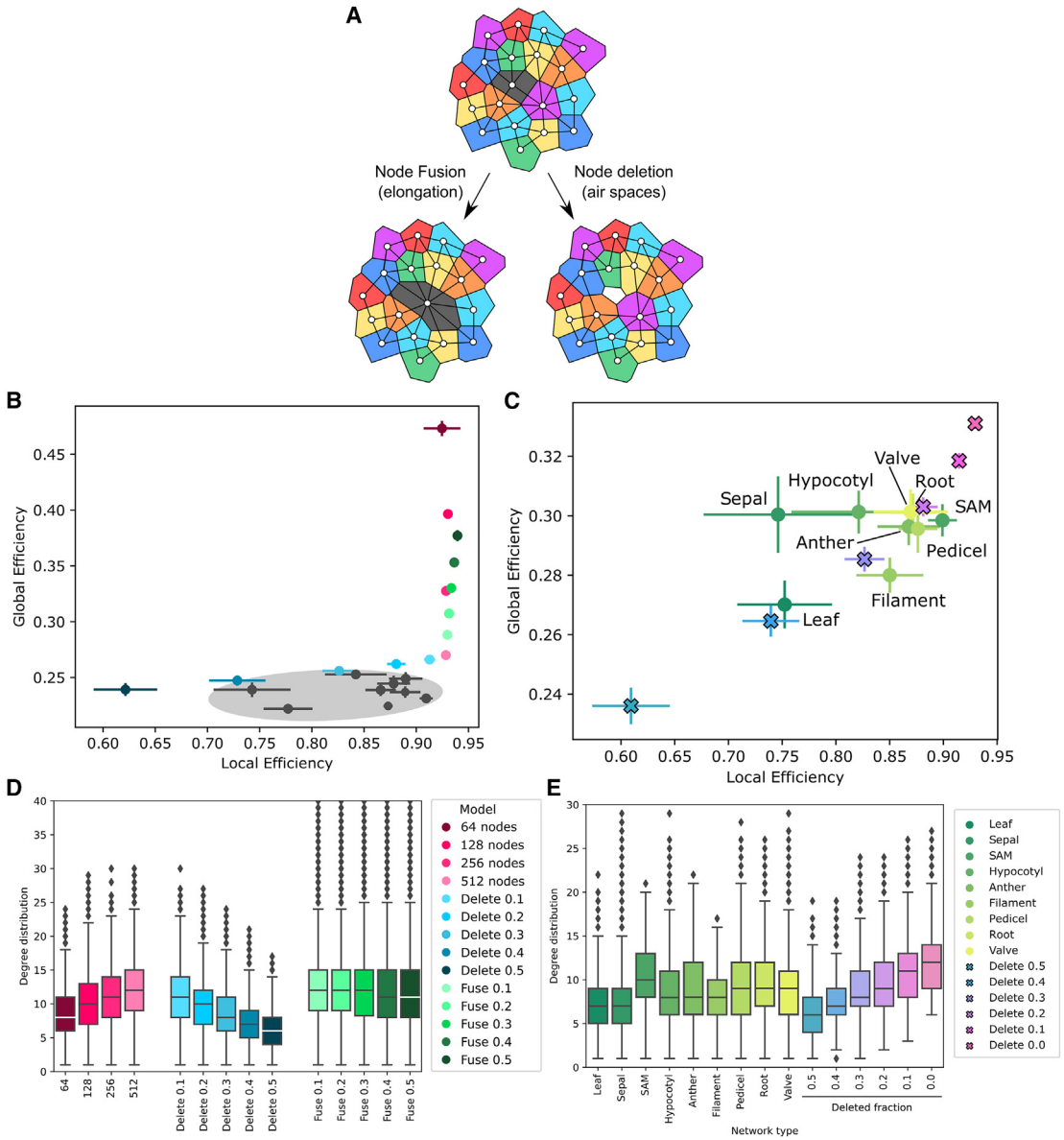

Figure 3. Quantitative comparison of *Arabidopsis* organs with default cellular configurations

Quantitative analysis of virtual organ models with randomly packed cells model

(A) Schematic representation of the fusion and deletion of nodes in model networks.

(B) Quantitative morphospace using global and local transport efficiency of randomly packed cells with increasing amounts of total cells (magenta), fractions of deleted cells (blue), or fused cells (green). All fusion and deletion templates are produced from the 512 cells model. *Arabidopsis* organ properties are shown within the gray shaded area and black points.

(C) Comparison of downsampled *Arabidopsis* organs (points) with synthetic networks with a fraction of deleted cells (crosses), with 256 final cells. Each data point in (B) and (C) corresponds to the average of 30 replicates of that model, with error bars extending to one standard deviation.

(D) Degree distributions of the randomly packed deletion and fusion models presented in (B).

(E) Comparison of degree distributions between downsampled real tissue networks from *Arabidopsis* organs and synthetic tissues, with varying degrees of node deletion presented in (C). (D and E) The boxplots show the quartiles of the dataset, whereas the whiskers extend to show the remainder of the distribution. See also Figures S3 and S4.

(Figures 3B and 3C). An overlap between some organs and models is observed. For instance, the SAM, root, valve, anther, filament, and pedicel are quite close to the networks generated with 20% of random deleted nodes (Figure 3C). The hypocotyl is close to 30% deletion, the leaf is close to 40% deletion, and the sepal is unmatched by models presented here.

Although deleting cells decreased the average degree in these networks (Figure 3D), this remained within the range of real plant tissues (Figure 3E). By contrast, random fusion of cells did not impact the overall degree distribution as much, predominantly creating outliers in distributions while leaving average values unchanged.

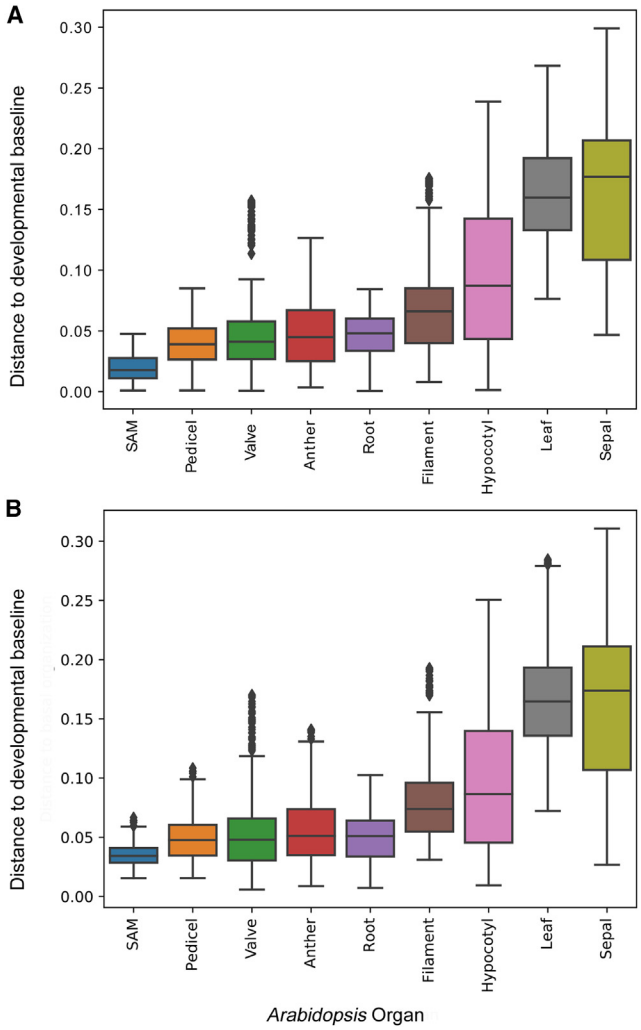

Figure 4. Distance of plant organ cellular configurations from default topological space

(A) Plot depicting the extent of deviation of *Arabidopsis* organs from a default organ design space. Using the 0.001 μm centroid noise method as a baseline model, pairwise Euclidean distances between different *Arabidopsis* organs in the local-global transport efficiency space are shown.

(B) Same as (A), using an 80 σ cell positional bias model developmental baseline. The boxplots show the quartiles of the dataset, whereas the whiskers extend to show the remainder of the distribution, except for points that are determined to be "outliers," using a method that is a function of the interquartile range.

Using the family of models using random and biased positioning of cell centroids as a starting point for node deletion and fusion analyses yielded common patterns as the noisy centroid starting point with respect to changes in degree and placement within the quantitative morphospace (Figure S4).

Distance of *Arabidopsis* organs to a topological developmental baseline

We sought to establish the extent to which the organization of cells in the diverse tissues of the model plant *Arabidopsis* deviates from the null-model configurations. In other words, to what extent are active patterning processes required to generate the cellular topologies observed across this plant?

Two models used were for comparison: the lattice noisy centroid (0.001 μm) and the biased centroid positioning (80 σ) models, based on their proximity to real plant organs (Figure 1C). For each of the plant organs, the Euclidean distance to each developmental baseline was measured and plotted (Figure 4).

A similar ranking of organ complexity is observed with both baseline models (Figures 4A and 4B). The *Arabidopsis* tissue closest to the developmental baseline is the SAM. The undifferentiated state of this pool of stem cells is therefore reflected by minimal topological complexity present in the cellular configuration.

Organs furthest from the developmental baseline included the leaf and the sepal. The generative processes needed to make these tissues, therefore, require the greatest amount of active developmental patterning. These are highly specialized tissues with airspaces that follow the specific functionality of the organ, a structural difference captured by network metrics that can be linked to their biological function. Such a difference in structure was captured with additional processes, namely the deletion of cells in our models.

DISCUSSION

Since the emergence of multicellular organisms, there has been a constant evolution of new cell types and structures, pushing the upper limits of organismal complexity.[1] The evolution of complexity is thought to be connected to the capacity to occupy new niches, expanding the biological range of multicellular organisms. This link also implies a relationship between structure and function, an idea that pervades much of biological theory.[7] The changes in structure can be composed of changes in the building blocks of tissues and organs, as well as the physical embedding and spatial arrangement of cells within them.

This study investigated the extent to which these configurations are generated by active patterning mechanisms versus topological features that emerge "for free" by virtue of cells being embedded in space. Using network science, we quantitatively compared properties of cellular order in real tissues (Figure 1) with "default" cellular patterns that arise in digital organ models (Figure 2).

From this analysis, a morphospace of organ design was constructed,[35] taking into consideration global transport optimization as well as local resilience to cellular failure. In this design space, both models and real plant tissues segregate into specific regions. Some parts of this morphospace occupied by real tissues cannot be reached with the null models and thus require invoking active patterning mechanisms that can further shape cell topologies. We model these mechanisms by introducing deletion and fusion of cells upon the synthetic networks created by the models. These processes are assumed to simulate the creation of airspaces[36,37] within a tissue as well as the presence of elongated cells and cell anisotropy.[31,33]

Following this examination, we conclude that there is a baseline of order given for free to organ connectomes by virtue of being composed of cells packed in 3D space. Simpler tissues, like the undifferentiated SAM,[19] deviate least from this default design paradigm, whereas other more specialized tissues deviate

further from this baseline complexity. The more specialized and "non-SAM-like" the tissue becomes, the more its local efficiency drops, suggesting tissue complexity comes at the cost of network robustness.

By contrast, normalized global efficiency remained relatively constant across all organs examined. The preservation of this property may reflect a mode of imparting resilience to organs, whereby the movement of pathogens, such as viruses, from cell to cell is hampered across these spatially and topologically constrained systems.

This creates a usable principle of how to obtain high-order network properties from local changes in topology. Such insight might prove valuable to those constructing non-natural organs and organoids from scratch and their use as models of disease,[38–40] especially since the capacity to fabricate 3D organs with 3D printing techniques has become a reality.[41,42] Using the design principles described here, tailored transport efficiencies and resiliencies to cellular failure can be obtained, paving the way for new biological tissues and organs with designed functionalities.

The 3D digital tissue atlas generated in this study provides a valuable resource to explore tissue complexity and 3D cell shapes in *Arabidopsis*. Toward this, cell types have been annotated within these represented datasets, enabling cell-type-specific analyses to be performed. The data have been used previously to demonstrate the efficacy of cell segmentation algorithms[43] and may also be used as 3D templates to run diverse simulations of transport and growth processes in different organs. Image and network data are freely available at https://osf.io/fzr56/.

STAR★METHODS

Detailed methods are provided in the online version of this paper and include the following:

- KEY RESOURCES TABLE
- RESOURCE AVAILABILITY
  - Lead contact
  - Materials availability
  - Data and code availability
- EXPERIMENTAL MODEL AND SUBJECT DETAILS
  - Arabidopsis growth conditions
  - Organ staining, clearing and imaging
  - Data preprocessing
  - Segmentation and generation of cellular connectivity networks
- METHOD DETAILS
  - 3D Voronoi models
  - Network extraction and analysis
  - Random positioning model
  - Centroid noise model
  - Biased centroid position model
  - Fusion and deletion of nodes in the models
  - Distance to default cellular configuration calculations
- QUANTIFICATION AND STATISTICAL ANALYSIS
  - Model replicates in synthetic organs
  - Subsampling of model networks and organ connectomes
  - Statistical details

SUPPLEMENTAL INFORMATION

Supplemental information can be found online at https://doi.org/10.1016/j.cub.2023.09.048.

ACKNOWLEDGMENTS

We thank Richard Smith (JIC) for support with MorphographX. G.W.B. and S.D.-N. were supported by Leverhulme grant no. RPG-2016-049, and G.W.B. was supported by BBSRC grant nos. BB/L010232/1, BB/J017604/1, and BB/N009754/1; a Turing Fellowship at The Alan Turing Institute; and a Human Frontiers in Science research grant RGP0002/2020.

AUTHOR CONTRIBUTIONS

Investigation and resources, S.D.-N. and M.D.B.J.; conceptualization, writing, and funding acquisition, G.W.B.

DECLARATION OF INTERESTS

The authors declare no competing interests.

Received: March 7, 2023
Revised: August 23, 2023
Accepted: September 20, 2023
Published: October 11, 2023

REFERENCES

1. Bonner, J.T. (1988). The Evolution of Complexity by Means of Natural Selection (Princeton University Press).
2. Bonner, J.T. (1998). The origins of multicellularity. Integrative Biology: Issues, News, and Reviews *1*, 27–36.
3. Michod, R.E. (2007). Evolution of individuality during the transition from unicellular to multicellular life. Proc. Natl. Acad. Sci. USA *104* (*Suppl 1*), 8613–8618.
4. Szathmáry, E., and Smith, J.M. (1995). The major evolutionary transitions. Nature *374*, 227–232.
5. Bonner, J.T. (2013). Randomness in Evolution (Princeton University Press).
6. Yanni, D., Jacobeen, S., Márquez-Zacarías, P., Weitz, J.S., Ratcliff, W.C., and Yunker, P.J. (2020). Topological constraints in early multicellularity favor reproductive division of labor. eLife *9*, e54348.
7. Thompson, D.W. (1942). On Growth and Form (Cambridge University Press).
8. White, J.G., Southgate, E., Thomson, J.N., and Brenner, S. (1986). The structure of the nervous system of the nematode Caenorhabditis elegans. Philos. Trans. R. Soc. Lond. B Biol. Sci. *314*, 1–340.
9. Bissell, M.J., and LaBarge, M.A. (2005). Context, tissue plasticity, and cancer: are tumor stem cells also regulated by the microenvironment? Cancer Cell *7*, 17–23.
10. Lamouille, S., Xu, J., and Derynck, R. (2014). Molecular mechanisms of epithelial–mesenchymal transition. Nat. Rev. Mol. Cell Biol. *15*, 178–196.
11. Wang, R.A., Li, Z.S., Zhang, H.Z., Zheng, P.J., Li, Q.L., Shi, J.G., Yan, Q.G., Ye, J., Wang, J.B., Guo, Y., et al. (2013). Invasive cancers are not necessarily from preformed in situ tumours—an alternative way of carcinogenesis from misplaced stem cells. J. Cell. Mol. Med. *17*, 921–926.
12. Jelier, R., Kruger, A., Swoger, J., Zimmermann, T., and Lehner, B. (2016). Compensatory cell movements confer robustness to mechanical deformation during embryonic development. Cell Syst. *3*, 160–171.
13. Song, H.-j., and Poo, M.-m. (2001). The cell biology of neuronal navigation. Nat. Cell Biol. *3*, E81–E88.
14. Coen, E., Rolland-Lagan, A.G., Matthews, M., Bangham, J.A., and Prusinkiewicz, P. (2004). The genetics of geometry. Proc. Natl. Acad. Sci. USA *101*, 4728–4735.

15. Yoshida, S., Barbier de Reuille, P.B., Lane, B., Bassel, G.W., Prusinkiewicz, P., Smith, R.S., and Weijers, D. (2014). Genetic control of plant development by overriding a geometric division rule. Dev. Cell *29*, 75–87.
16. Ramon y Cajal, S. (1911). Histologie du système nerveux de l'homme et des vertébrés*2* (Maloine), pp. 153–173.
17. Bullmore, E., and Sporns, O. (2009). Complex brain networks: graph theoretical analysis of structural and functional systems. Nat. Rev. Neurosci. *10*, 186–198.
18. Bassel, G.W. (2019). Multicellular systems biology: quantifying cellular patterning and function in plant organs using network science. Mol. Plant *12*, 731–742.
19. Jackson, M.D.B., Duran-Nebreda, S., Kierzkowski, D., Strauss, S., Xu, H., Landrein, B., Hamant, O., Smith, R.S., Johnston, I.G., and Bassel, G.W. (2019). Global topological order emerges through local mechanical control of cell divisions in the Arabidopsis shoot apical meristem. Cell Syst. *8*, 53–65.e3.
20. Jackson, M.D., Xu, H., Duran-Nebreda, S., Stamm, P., and Bassel, G.W. (2017). Topological analysis of multicellular complexity in the plant hypocotyl. eLife *6*, e26023.
21. Kauffman, S.A. (1993). The Origins of Order: Self-Organization and Selection in Evolution (Oxford University Press).
22. Du, Q., and Wang, D. (2003). Tetrahedral mesh generation and optimization based on centroidal Voronoi tessellations. Int. J. Numer. Methods Eng. *56*, 1355–1373.
23. Jackson, M.D.B., Duran-Nebreda, S., and Bassel, G.W. (2017). Network-based approaches to quantify multicellular development. J. R. Soc. Interface *14*, 20170484.
24. Latora, V., and Marchiori, M. (2001). Efficient behavior of small-world networks. Phys. Rev. Lett. *87*, 198701.
25. Cardillo, A., Scellato, S., Latora, V., and Porta, S. (2006). Structural properties of planar graphs of urban street patterns. Phys. Rev. E Stat. Nonlin. Soft Matter Phys. *73*, 066107.
26. Jerauld, G.R., Scriven, L.E., and Davis, H.T. (1984). Percolation and conduction on the 3D Voronoi and regular networks: a second case study in topological disorder. J. Phys. C: Solid State Phys. *17*, 3429–3439.
27. de Reuille, P.B., Routier-Kierzkowska, A.-L., Kierzkowski, D., Bassel, G.W., Schüpbach, T., Tauriello, G., Bajpai, N., Strauss, S., Weber, A., and Kiss, A. (2015). MorphoGraphX: a platform for quantifying morphogenesis in 4D. eLife *4*, e05864.
28. Barabási, A.L., and Albert, R. (1999). Emergence of scaling in random networks. Science *286*, 509–512.
29. Papadopoulos, L., Porter, M.A., Daniels, K.E., and Bassett, D.S. (2018). Network analysis of particles and grains. J. Complex Netw. *6*, 485–565.
30. Dolan, L., Janmaat, K., Willemsen, V., Linstead, P., Poethig, S., Roberts, K., and Scheres, B. (1993). Cellular organisation of the Arabidopsis thaliana root. Development *119*, 71–84.
31. Roeder, A.H., Chickarmane, V., Cunha, A., Obara, B., Manjunath, B.S., and Meyerowitz, E.M. (2010). Variability in the control of cell division underlies sepal epidermal patterning in Arabidopsis thaliana. PLoS Biol. *8*, e1000367.
32. Hamant, O., Heisler, M.G., Jönsson, H., Krupinski, P., Uyttewaal, M., Bokov, P., Corson, F., Sahlin, P., Boudaoud, A., Meyerowitz, E.M., et al. (2008). Developmental patterning by mechanical signals in Arabidopsis. Science *322*, 1650–1655.
33. Sapala, A., Runions, A., Routier-Kierzkowska, A.L., Das Gupta, M.D., Hong, L., Hofhuis, H., Verger, S., Mosca, G., Li, C.B., Hay, A., et al. (2018). Why plants make puzzle cells, and how their shape emerges. eLife *7*, e32794.
34. Lehmeier, C., Pajor, R., Lundgren, M.R., Mathers, A., Sloan, J., Bauch, M., Mitchell, A., Bellasio, C., Green, A., Bouyer, D., et al. (2017). Cell density and airspace patterning in the leaf can be manipulated to increase leaf photosynthetic capacity. Plant J. *92*, 981–994.
35. Ollé-Vila, A., Duran-Nebreda, S., Conde-Pueyo, N., Montañez, R., and Solé, R. (2016). A morphospace for synthetic organs and organoids: the possible and the actual. Integr. Biol. (Camb) *8*, 485–503.
36. Dolan, L., Linstead, P., and Roberts, K. (1997). Developmental regulation of pectic polysaccharides in the root meristem of Arabidopsis. J. Exp. Bot. *48*, 713–720.
37. Lightner, J., James, D.W., Jr., Dooner, H.K., and Browse, J. (1994). Altered body morphology is caused by increased stearate levels in a mutant of Arabidopsis. Plant J. *6*, 401–412.
38. Clevers, H. (2016). Modeling development and disease with organoids. Cell *165*, 1586–1597.
39. Fatehullah, A., Tan, S.H., and Barker, N. (2016). Organoids as an in vitro model of human development and disease. Nat. Cell Biol. *18*, 246–254.
40. Lancaster, M.A., Renner, M., Martin, C.A., Wenzel, D., Bicknell, L.S., Hurles, M.E., Homfray, T., Penninger, J.M., Jackson, A.P., and Knoblich, J.A. (2013). Cerebral organoids model human brain development and microcephaly. Nature *501*, 373–379.
41. Mironov, V. (2003). Printing Technology to Produce Living Tissue (Taylor & Francis).
42. Mironov, V., Kasyanov, V., and Markwald, R.R. (2011). Organ printing: from bioprinter to organ biofabrication line. Curr. Opin. Biotechnol. *22*, 667–673.
43. Wolny, A., Cerrone, L., Vijayan, A., Tofanelli, R., Barro, A.V., Louveaux, M., Wenzl, C., Strauss, S., Wilson-Sánchez, D., Lymbouridou, R., et al. (2020). Accurate and versatile 3D segmentation of plant tissues at cellular resolution. eLife *9*, e57613.
44. Truernit, E., Bauby, H., Dubreucq, B., Grandjean, O., Runions, J., Barthélémy, J., and Palauqui, J.C. (2008). High-resolution whole-mount imaging of three-dimensional tissue organization and gene expression enables the study of phloem development and structure in Arabidopsis. Plant Cell *20*, 1494–1503.
45. Bassel, G.W. (2015). Accuracy in quantitative 3D image analysis. Plant Cell *27*, 950–953.
46. Montenegro-Johnson, T.D., Stamm, P., Strauss, S., Topham, A.T., Tsagris, M., Wood, A.T., Smith, R.S., and Bassel, G.W. (2015). Digital single-cell analysis of plant organ development using 3DCellAtlas. Plant Cell *27*, 1018–1033.
47. Hagberg, A., Swart, P., Chult, S., and D. (2008). Exploring network structure, dynamics, and function using NetworkX. In SCIPY 08 (Los Alamos National Lab [LANL]).
48. Bassel, G.W., Stamm, P., Mosca, G., Barbier de Reuille, P.B., Gibbs, D.J., Winter, R., Janka, A., Holdsworth, M.J., and Smith, R.S. (2014). Mechanical constraints imposed by 3D cellular geometry and arrangement modulate growth patterns in the Arabidopsis embryo. Proc. Natl. Acad. Sci. USA *111*, 8685–8690.
49. Newman, M.E.J. (2005). A measure of betweenness centrality based on random walks. Soc. Netw. *27*, 39–54.
50. Freeman, L.C. (1977). A set of measures of centrality based on betweenness. Sociometry *40*, 35–41.
51. Korf, R.E. (1985). Depth-first iterative-deepening: an optimal admissible tree search. Artif. Intell. *27*, 97–109.

STAR★METHODS

KEY RESOURCES TABLE

REAGENT or RESOURCE	SOURCE	IDENTIFIER
Deposited data		
Scripts	This work	https://doi.org/10.5281/zenodo.8322918
		https://doi.org/10.5281/zenodo.8322918
Organ data	https://osf.io/fzr56/	https://doi.org/10.17605/osf.io/fzr56
Model data	https://osf.io/k2npx/	https://doi.org/10.17605/OSF.IO/K2NPX
Software and algorithms		
MorphoGraphX	https://morphographx.org/	Version 2.0.1
ITK library	https://morphographx.org/software/	Version 5.1.2
Cuda toolkit	http://developer.nvidia.com/category/zone/cuda-zone	Version 11.4
NetworkX	https://networkx.org/	Version 1.1
Python	https://www.python.org/	Version 3.9
MeshLab	https://www.meshlab.net/	Version 2020.3

RESOURCE AVAILABILITY

Lead contact

Further information and requests for resources should be directed to and will be fulfilled by the lead contact, George Bassel (george.bassel@warwick.ac.uk)

Materials availability

This study did not generate new unique reagents.

Data and code availability

- Data generated in this study has been deposited to the *osf* repositories https://osf.io/fzr56/ and https://osf.io/k2npx/.
- All original code has been deposited at Zenodo at https://doi.org/10.5281/zenodo.8322918 and is publicly available as of the date of publication.
- DOIs are listed in the key resources table.

EXPERIMENTAL MODEL AND SUBJECT DETAILS

Arabidopsis growth conditions

Arabidopsis plants were grown in soil (2:1:1, peat:pearlite:vermiculite) under glasshouse conditions with 16 h light (23°C) and 8 h dark, at 22 °C under glasshouse conditions. Samples from mature plants were collected and placed directly into the fixative 3:1 ethanol:acetic.

Organ staining, clearing and imaging

Cell walls were stained using the mPA-PI method as previously described.[20,44] Stained samples were placed in a 35 mm Cellview Cell Culture Dish (Greiner, UK) and mounted in chloral hydrate clearing solution (4 g chloral hydrate, 1 mL glycerol, 2 mL water). Tissues were imaged using an inverted Zeiss LSM710 Confocal with a 25X Oil immersion lens.

Data preprocessing

Prior to cell segmentation, image stacks were normalized in MorphoGraphX[27] using the ITK plugin Normalize Stack with settlings X, Y, Z radius 25, X, Y, Z σ = 0.5, Threshold = 50 and Blur factor = 0.7. A Gaussian Blur was next applied to the image with a radius of 0.3-0.5, depending on the tissue.

Polygonal meshes capturing cell surfaces were generated using the 3D Marching Cubes algorithm, with a cube size ranging from 0.7-1.0 depending on the tissue, followed by 30 smooth passes at the time of the mesh creation to preserve cellular connectivity.[45]

Segmentation and generation of cellular connectivity networks

An ITK autoseeded watershed was applied to segment the cells of tissues in 3D (www.itk.org). The outputs of this process were manually curated to ensure accuracy and fuse multiple segments representing individual cells. Segmented cells were used for both geometric analyses and polygonal meshes for topological analyses, as outlined below.

Topological analyses of cellular connectivity were performed on segmented organs using the generated polygonal meshes and the algorithm included in 3DCellAtlas.[46] Entire segmented organs were topologically analysed, however only a subset of the cells within this tissue, representing regions which were segmented to the highest quality were reported on. Additional cells between the analysed portion of the tissue and sample boundary provided a topological buffering which limit the impact of edge effects due to the incomplete imaging of whole organs (Figure S3).[19,20] Cell interfaces less at 1 μm^2 were removed from the network as this may arise due to noise present in the image acquisition and analysis pipeline. Topological analyses of cellular connectivity were performed using NetworkX in Python.[47]

METHOD DETAILS

3D Voronoi models

Voronoi models were generated computationally placing centroid positions using MorphoGraphX,[27] which were used in Voronoi tessellation within a bounding mesh.[22] Centroids were then imported into MorphoGraphX using the 'Load Point Cloud' process in CellMaker.[27,48] Surface meshes were created using the CellMaker in order to prevent centroids on the surface of the model from growing infinitely in Voronoi tessellation due to lack of a boundary. With both centroids and a surface mesh loaded, 3D Voronoi tessellation of points was then carried out using the 'Voronoi Cells from Point Cloud' process (relevant parameters: cage points = 1000, minimum distance cage points = 1.0, threshold merging = 0.01).

Network extraction and analysis

Cellular connectivity networks of virtual and real segmented organs were extracted in MorphoGraphX.[46] Edge lists were produced and imported into Python as an undirected network using the NetworkX library.[47] Graph objects in NetworkX are stored as adjacency dictionaries for fast lookup and data manipulation. Node network measures were computed using standard NetworkX functions.[47,49] In the case of betweenness centrality,[50] all data shown corresponds to the log transform of the original measures. Global and local efficiencies were calculated using a Python script using NetworkX (version 1.1), following the formula and process described in Latora and Marchiori.[24]

Random positioning model

Centroids were computationally positioned in a cube with random coordinates following a uniform distribution using MorphoGraphX. This cube had double the length, width and height of the target sphere radius. Centroids falling outside of the sphere were rejected, while centroids inside of the sphere were accepted, until the desired number of centroids was reached (from 4 to 512 nodes). This point cloud of centroids was then 3D tessellated using the Voronoi tessellation process.[22] 30 replicate models were created for each set of parameters used.

Centroid noise model

A regular lattice configuration spanning a target-sized sphere was pre-computed and used as the starting point for this family of models. This lattice was generated using Python following a triangular conformation with 12 edges per node. To this point cloud of orderly placed centroids, increasing amounts of positional noise were applied, using a uniform distribution of specified range (from +/-0.001 μm to +/-4 μm). Upon this transformation, the point cloud was tessellated using 3D Voronoi tessellation.[22] 30 replicate models were created for each set of parameters used.

Biased centroid position model

Using MorphoGraphX, Centroids 3D coordinates were generated using a Gaussian distribution with mean set to the boundary of the target sphere. Centroids falling outside of the sphere were rejected, while centroids inside of the sphere were accepted, until the desired number of centroids was reached (512 nodes). The usage of a Gaussian distribution instead of a uniform distribution led to the creation of different regions within the sphere: close to the mean of the 3D Gaussian distribution centroids were tightly packed, while on the other end of the point cloud centroids were located further apart. As a control parameter, the σ of the normal distribution was used to control the bias in the positioning of the nodes: with high spread the Gaussian distribution more closely resembles a uniform distribution, while at lower spreads the bias is accentuated. This way, the 3D Voronoi tessellation gives rise to a wider range of cell sizes (Figure S3). 30 replicate models were created for each set of parameters used.

Fusion and deletion of nodes in the models

Fusion of nodes was addressed by random choice of a node and merge of that node with a randomly (uniformly) chosen neighbor. In this way, all the previous node's connections are inherited by the second. This was carried out until a given fraction of nodes had been fused. In a similar manner, random deletion was carried out by removing a node and its edges from the graph, chosen using a random

uniform distribution from the graph's set, until a given fraction of nodes had been removed. Due to the impact of network fragmentation into global efficiency calculations, only fully connected networks were considered for further analysis.

Distance to default cellular configuration calculations

To compute the distance of each tissue to these baseline configurations, a Euclidean distance was used using two dimensions, local efficiency and global efficiency, following the formula:

$$D = \sqrt{\left[(L_{E1} - L_{E2})^2 + (G_{E1} - G_{E2})^2\right]}$$

Where D stands for the topological distance between each of the topological datasets and LE and GE stand for local and global efficiency, respectively.

QUANTIFICATION AND STATISTICAL ANALYSIS

Model replicates in synthetic organs

30 independently produced replicate organs were used for each of the models and set of parameters used.

Subsampling of model networks and organ connectomes

To compare networks obtained by node deletion, starting templates were downscaled by removing the outer layer cells from the starting 512 cell model. The outer-inner location of the nodes was identified by their degree, with lower degree nodes being present on the outer edge of the graph. The subsampling was performed so that after removing a given fraction of nodes by random deletion, the resulting graph would remain at 256 cells and thus be comparable to both the real organ and model connectomes downscaled to the same size.

To compare biological organ networks with differing sizes, connectomes for each *Arabidopsis* organ were subsampled to defined sizes. Starting from a random node in the graph, a breadth-first search algorithm[51] was used to choose a 256-node sized connected subgraph. This process was repeated 30 times to obtain independent replicates, which were later processed by calculating their respective local and global efficiencies, and other network measures.

Statistical details

Boxplots in this article show the mean value of the distribution as a central line within the box. The limits of the box represent the quartiles of the distribution while the whiskers extend to show the remainder of the sample. Outlier points were determined using the inter-quartile range method.

For all distributions shown in the quantification of organs and models, each data point corresponds to the mean value of 30 replicates, with error bars extending to one standard deviation of the distribution from the average value.